Orbital effects and Affleck-Haldane-type spin dimerization in $Ba_4Ru_3O_{10}$

J. Sannigrahi,[1,2] A. Paul,[3,4] A. Banerjee,[4] D. Khalyavin,[2] A. D. Hillier,[2] K. Yokoyama,[2] A. K. Bera,[5] M. R. Lees,[6] I. Dasgupta,[4] S. Majumdar,[4,*] and D. T. Adroja[2,7]

[1]*Department of Physics, University of Loughborough, Loughborough LE11 3TU, United Kingdom*
[2]*ISIS Neutron and Muon Source, Science and Technology Facilities Council, Rutherford Appleton Laboratory, Didcot OX11 0QX, United Kingdom*
[3]*Department of Chemistry, Bar-Ilan University, Ramat Gan 5290002, Israel*
[4]*School of Physical Sciences, Indian Association for the Cultivation of Science, 2A & B Raja S. C. Mullick Road, Jadavpur, Kolkata 700 032, India*
[5]*Solid State Physics Division, Bhabha Atomic Research Centre, Mumbai 400085, India*
[6]*Department of Physics, University of Warwick, Coventry CV4 7AL, United Kingdom*
[7]*Highly Correlated Matter Research Group, Physics Department, University of Johannesburg, Auckland Park 2006, South Africa*

(Received 2 September 2020; accepted 8 April 2021; published 26 April 2021)

$Ba_4Ru_3O_{10}$, the quasi-one-dimensional spin-1 ($S = 1$) compound, has rather intricate magnetic properties. The compound consists of structural Ru trimers, which together form the zig-zag chains where the Ru has two inequivalent crystallographic sites. While at high temperature both the inequivalent Ru ions stay in the 4+ state with effective $S = 1$ spin state, upon lowering the temperature, the magnetic moment of the central Ru atom is completely quenched accompanied by a change in the octahedral environment. This effectively gives rise to a bond-alternating chain and provides an opportunity to study the excitation of such a spin network in a real material. We have used microscopic tools such as neutron scattering and muon spin relaxation along with the density functional theory based calculations to address the spin state of the two inequivalent Ru ions in this material. From our neutron powder diffraction, on lowering of temperature, we find a large tetragonal distortion of the central RuO_6 octahedra of the trimer. The splitting of the t_{2g} level of the central Ru due to this distortion is found to be significant leading to the quenching of the moment underscoring the Hund's exchange. The nonmagnetic central Ru promotes a strong antiferromagnetic superexchange between the other two Ru ions in the trimer, which gives rise to a dimeric state. The presence of spin dimers is reflected by the manifestation of a gap in the spin excitation spectra. The spin-dimer formation in $Ba_4Ru_3O_{10}$ is at par with the effective model proposed by Affleck and Haldane for the $S = 1$ bond alternating chains in the light of valence bond solid formalism. Eventually, at a lower temperature, a long-range ordered antiferromagnetic state emerges from the gapped dimer state due to the significant interdimer interactions.

DOI: 10.1103/PhysRevB.103.144431

I. INTRODUCTION

One-dimensional integer spin antiferromagnetic (AFM) Heisenberg systems have several unique properties in comparison to their half-integer counterparts [1–6]. These includes the existence of a nondegenerate gapped ground state (Haldane gap) [7,8], exotic string correlations reflecting a hidden topological order [9,10], large-D phase in the presence of significant spin anisotropy [11–14], and the valence bond solid state with quantum entanglement [15]. For the case of a bond alternating $S = 1$ chain having consecutive exchange interactions J_1 and J_2, a quantum phase transition from the uniform Haldane phase to an Affleck-Haldane-type dimer phase occurs upon increasing the strength of the alternating bond parameter, $\alpha = (J_1 - J_2)/(J_1 + J_2)$ [1,16–18]. Here, both the phases are gapped, and the gap vanishes only at a critical value of α, $\alpha_c \sim 0.25$. Most of the $S = 1$ spin systems studied so far are Ni-based compounds [19–23]. Additionally, an $S = 1$ state can be realized in Ru^{4+} ions when only the low lying t_{2g} levels are occupied [24–26]. In this context, $Ba_4Ru_3O_{10}$ (BRO) is an ideal testbed for the various theoretically proposed phases for $S = 1$ spin chains.

The unit cell of BRO is orthorhombic base-centered with the space group *Cmca* and contains two inequivalent Ba sites, two inequivalent Ru sites, and four inequivalent O sites [27–29]. The structure is built out of Ru_3O_{12} trimers, which are formed by three face sharing RuO_6 octahedra (see Fig. 1). The two Ru atoms, Ru(1) and Ru(2), occupy the middle and outer positions of the trimer, respectively. Such trimeric building blocks are connected to the other such adjacent blocks by corner sharing. This arrangement leads to the formation of zigzag chains of $Ru(2)O_6$ octahedra running along the c axis [30].

While BRO orders antiferromagnetically below T_N=107 K [29], we find Affleck-Haldane-type spin-dimer formation in the temperature range $T_N < T < T_P$, where T_P is close to 400 K. The strong dimerization of Ru(2) ions in a trimer

*sspsm2@iacs.res.in

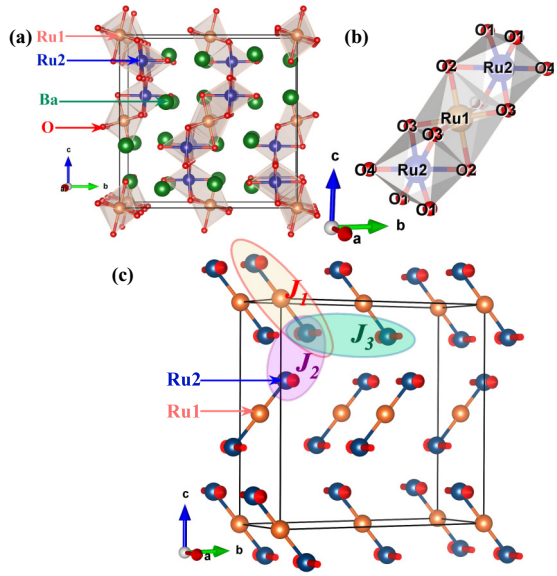

FIG. 1. (a) View of the crystal structure of $Ba_4Ru_3O_{10}$. (b) Face shared octahedra in Ru_3O_{12} trimer. (c) Magnetic structure of BRO as obtained from our neutron powder diffraction data. Here J_1, J_2 and J_3 represent the intradimer, interdimer and interlayer magnetic exchange interaction terms, respectively.

is promoted by the middle Ru(1) ions which become nonmagnetic. Density functional theory (DFT) [30,31] and bond valence method calculations [32] envisaged that the zero (ordered) moment at the Ru(1) site originates from the charge disproportionation between Ru ions and the formation of molecular orbitals (MOs) in the Ru trimer. Nevertheless, the microscopic origin of zero moment state of Ru(1) remains elusive, as the MO theory may not be enough to predict the moment at a single atomic site. In addition, there are almost no reports on the spin excitations in such nonuniform zig-zag chains providing an opportunity to access the $\Delta - \alpha$ phase diagram (Δ is the spin gap) for the $S = 1$ spin system (see Fig. A of the Supplemental Material [33]). Here, we have addressed all these issues through high-resolution neutron powder diffraction (NPD), muon spin relaxation (μSR), and inelastic neutron scattering (INS), which are supported by the DFT calculations. Our work establishes that the moment at the Ru(1) site vanishes well above T_N due to the effect of orbital ordering at the Ru sites promoted by a structural distortion. More strikingly, we observe a gap ($\approx$7 meV) in the spin excitation spectra above T_N which indicates a dimerized state of the Affleck-Haldane model [34]. Eventually, at a lower temperature, the interdimer interaction promotes long-range ordering.

II. METHODOLOGY

A polycrystalline sample of BRO was synthesized by a solid-state reaction route [27,28]. The powder x-ray diffraction pattern at room temperature showed the sample to be single phase with no signs of additional peaks. The magnetic measurements were carried out using a Quantum Design superconducting quantum interference device magnetometer (2–750 K) as well as using a vibrating sample magnetometer. The heat capacity was measured by relaxation technique using a Quantum Design Physical Property Measurement System.

The neutron powder diffraction, the inelastic neutron scattering, and the muon spin relaxation measurements were performed at the ISIS Facility of Rutherford Appleton Laboratory, United Kingdom. The NPD data were collected at different temperatures within the range 1.5 to 300 K using the WISH time-of-flight diffractometer. The powder sample of BRO was mounted in an 8-mm diameter vanadium can and cooled down to 1.5 K using a standard He cryostat. The thermal evolution of the crystal and magnetic structures are investigated by NPD at several temperatures below and above T_N. The Reitveld refinements of the diffraction patterns were performed using the Fullprof software package [35]. The analysis confirms that BRO crystallizes with orthorhombic symmetry (space group *Cmca*) with lattice parameters $a = 5.767(3)$ Å, $b = 13.245(2)$ Å, and $c = 13.064(4)$ Å at room temperature, which are consistent with a previous report [29]. It is to be noted that Dussarrat *et al.* [27] adopted a monoclinic space group ($P2_1/1$) for BRO. However, we do not see any splitting or broadening of the (111) and (112) reflections (in the orthorhombic indexing) even in the high resolution detector banks, indicating the absence of monoclinic distortion in the sample within the accuracy of the measurements ($\Delta d/d = 0.003$, where d is the lattice spacing).

The μSR measurements were performed using the EMU spectrometer in a longitudinal geometry [36]. The powder sample of BRO was mounted on a high purity Ag plate and covered by a thin layer of mylar film. The sample was cooled down to 2 K in He-exchange gas using a Variox cryostat from Oxford Instruments and the data were collected in the temperature range 2 to 120 K while heating.

INS measurements were carried out using the MERLIN time-of-flight chopper spectrometer [37]. The sample was placed in an aluminium foil packet in the form of an annulus of diameter 40 mm and height 40 mm and sealed in a thin aluminium can, which was cooled in He-exchange gas using a closed cycle refrigerator down to a base temperature of 4.5 K. The data were collected at 5, 50, 90, 130, 225, and 300 K with neutrons of incident energy $E_i = 100$ meV and a 350 Hz chopper frequency in a repetition-rate multiplication model, which also gave data for $E_i = 38$, 20, and 12 meV. To obtain the scattering intensity in the units of cross section, mb $sr^{-1}meV^{-1}f.u.^{-1}$, vanadium spectra were recorded in identical conditions. Simulations of the spin-wave excitations were performed using the SpinW software package [38].

All the electronic structure calculations presented in this paper were performed in the framework of density functional theory within the generalized gradient approximation (GGA) [39] including a Hubbard onsite d-d Coulomb interaction [40] as implemented in the Vienna *ab initio* simulation package [41,42]. The interactions between electrons and ions were incorporated by the projector augmented wave method [43,44]. The effective on-site Coulomb interaction for the Ru sites was taken to be 2 eV. The k-space integration in the Brillouin zone was carried out using the tetrahedron method with a $10\times10\times6$ Γ-centered k mesh. To calculate the on-site energy, a low-energy tight-binding Hamiltonian was constructed within the Wannier function basis using N^{th}-order muffin-tin

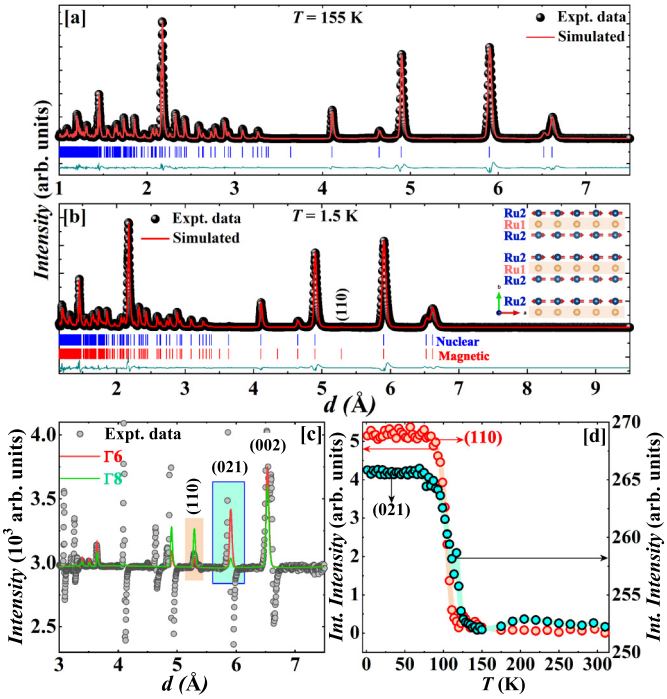

FIG. 2. NPD data collected at at (a) 155 K and (b) 1.5 K. Inset of (b) shows the magnetic structure as viewed along the *c*-axis. (c) Difference curve between 1.5 and 155 K data along with refinement curves (solid lines) using the Γ_6 and Γ_8 magnetic structures. (d) Temperature variation of the integrated intensities of (021) and (110) reflections.

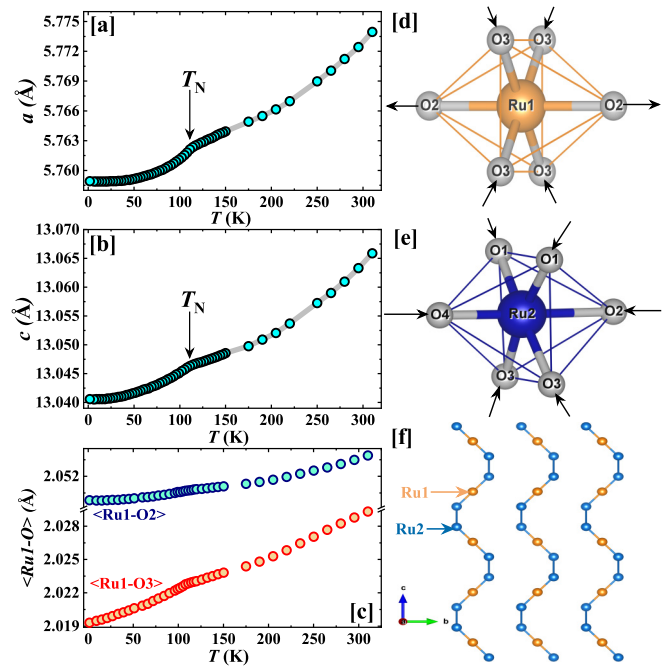

FIG. 3. Temperature dependence of the (a) a axis and (b) c axis lattice parameter. (c) Temperature variation of the ⟨Ru(1)-O⟩ distance in the middle octahedra for the two different O sites (O2 and O3). Schematic showing the shrinking of the (d) Ru(1)O6 and (e) Ru2O6 octahedra. (f) Zig-zag spin chains running along the *c* axis.

orbital downfolding method [45,46], as implemented in the Stuttgart linear-tin orbital code [47,48].

III. RESULTS AND DISCUSSIONS

A. Neutron powder diffraction

The full NPD pattern of BRO at 155 and 1.5 K, obtained from the low-scattering angle detector banks, are shown in Figs. 2(a) and 2(b). The difference between the NPD diffractograms at 1.5 and 155 K (below and above T_N, respectively) reveals an additional resolution limited Bragg peak [(110), forbidden in the space group *Cmca*] as well as an increase of the intensity of two nuclear peaks [(021) and (002)] [Fig. 2(c)]. The additional intensities are observed only at a large *d*-spacing region ($d > 3$ Å) pointing to their magnetic origin. All the magnetic reflections can be indexed using the $\mathbf{k} = (0\ 0\ 0)$ propagation vector consistent with the previous NPD study [29]. The previous study was limited to the observation of only the single magnetic reflection (002) which could not differentiate between Γ_6 (moment along the *a* axis) and Γ_8 (moments along the *b* axis) models. Our data clearly reveal that the moment along the *a* axis (i.e., Γ_6) provides a very accurate fitting of this reflection [Fig. 2(c)]. In addition, it also predicts a sizable contribution to the (021) reflection at low temperature, which lies on top of the nuclear peak. We integrated the (021) reflection (nuclear + magnetic) and plotted it as a function of temperature [Fig. 2(d)]. The temperature dependence of the integrated intensity revealed a clear critical behavior pointing to the presence of a measurable magnetic contribution. This is again consistent with the moment being along the *a* axis. The ordered magnetic moment per Ru(2) atom obtained from the refinement is 0.89(1) μ_B/Ru.

The temperature dependence of the NPD data indicate that there is no symmetry lowering down to 1.5 K. However, a clear anomaly is observed in the lattice parameters at T_N [Figs. 3(a) and 3(b)]. We have calculated the Ru-O bond lengths for both $Ru(1)O_6$ and $Ru(2)O_6$ octahedra and the Ru(1)-O3 and Ru(1)-O2 distances are plotted in Fig. 3(c). Here O2 and O3 are the oxygen atoms at the axial and equatorial positions of the Ru(1) octahedra, respectively [Fig. 3(d)]. The Ru(1)-O3 distance is *significantly larger* than the Ru(1)-O2 distance and this difference in the distances turns out to be more pronounced with the lowering of the temperature. It gives rise to a *significant tetragonal distortion* in the $Ru(1)O_6$ octahedra. The distortion is less prominent in $Ru(2)O_6$, because the change in metal-oxygen bond distance is more isotropic [Fig. 3(e)]. Such subtle structural differences in the $Ru(1)O_6$ and $Ru(2)O_6$ octahedra are found to be instrumental in determining the magnetic state of the compound (see also Fig. C in the Supplemental Material [33]).

B. μ^+ spin rotation

μSR provides a complementary tool for further probing the local magnetic order due to the large gyromagnetic ratio of the muon ($\gamma_\mu = 851.615$ MHz/T). The zero-field μSR data show well-defined oscillations below $T_N \sim 107$ K, indicating the long-range ordered state [Figs. 4(a) and 4(b)]. The oscillations disappear as we heat the sample above T_N [see 110 K data in Fig. 4(c)]. We have provided the distribution of the internal magnetic field B_{int} considering all the muon

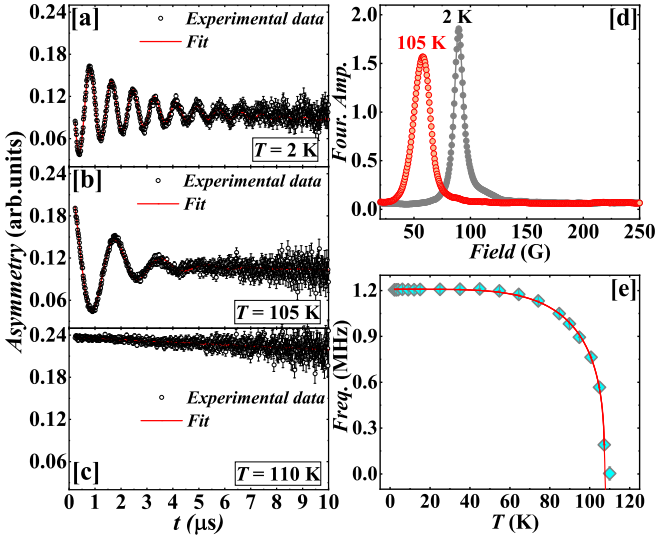

FIG. 4. (a)–(c) μSR data at different temperatures along with the fitting (see text). (d) Fourier amplitude of the muon asymmetry as a function of the internal field. (e) Muon precession frequency as a function of temperature along with a power-law fitting (see text).

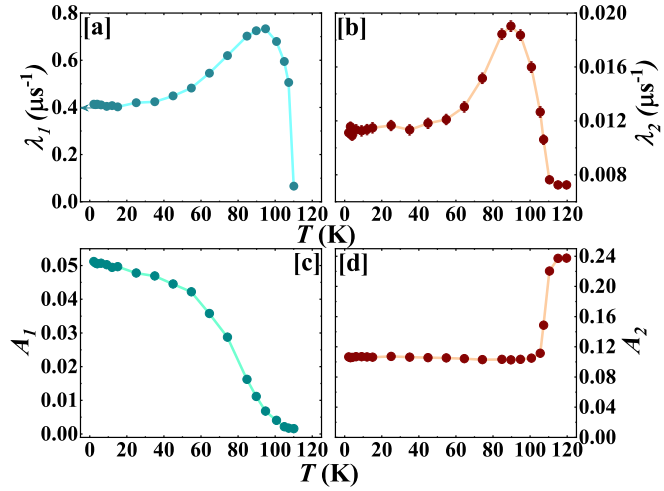

FIG. 5. Temperature variation of the two muon spin relaxation rates (a) λ_1 (fast) and (b) λ_2 (slow). Corresponding variation of the amplitude (c) A_1 and (d) A_2 with temperature.

sites based on the maximum entropy calculations using the muon polarization asymmetry [Fig. 4(d)]. It shows a single, quite well-peaked field distribution indicating that the muons are experiencing a single quasistatic local field. The resultant temperature dependence of the extracted muon precession frequency (ν) below T_N is representative of the magnetic order parameter and is described by the phenomenological power law: $\nu(T) = \nu(0)[1 - (T/T_N)^{\sigma}]^{\beta}$ [49]. The exponent σ corresponds to the low temperature properties that are governed by the magnon excitations, while β determines the asymptotic behavior of the zero-field magnetization near T_N. We obtain a rather good fit of our data to the above function [Fig. 4(e)] and the values of the parameters obtained from fitting are, $T_N = 108.0(1)$ K, $\nu(0) = 1.21(1)$ MHz, $\beta = 0.37(1)$ and $\sigma = 4.78(16)$. The value of β is close to 0.38 expected for a three-dimensional (3D) Heisenberg system.

The time-domain μSR data below T_N were fitted by using the equation:

$$G_z(t) = A_1 \exp(-\lambda_1 t)\cos(2\pi\nu t + \phi) + A_2 \exp(-\lambda_2 t) + A_{bg}. \quad (1)$$

Here A_i is the amplitude of the i-th component, λ_i is the corresponding relaxation rate, and ϕ is the phase angle. A_{bg} is the temperature independent part. The slow and fast relaxation rates λ_1 and λ_2, respectively, show a similar type of temperature dependence as shown in Figs. 5(a) and 5(b). They tend to level off at the values $\sim$0.4 and 0.2 μs^{-1} at the base temperature, respectively. The peak seen near T_N is due to the critical fluctuations associated with the magnetic transition. The temperature variation of A_1 shows an increase as the sample is cooled below T_N due to the enhanced amplitude of the oscillations [Fig. 5(c)]. On the other hand the paramagnetic component A_2 shows a sharp drop below T_N [shown in Fig. 5(d)] with the advent of long-range order, which indicates the absence of residual paramagnetism below T_N.

C. DFT study

We reexamined the electronic structure of BRO using first-principles DFT calculations. While the gross features of calculation are in agreement with the previously reported results [30,31], there are subtle differences which are crucial to understanding the magnetic properties of BRO. The t_{2g}-e_g crystal field splitting (Δ_{CF}) for the Ru(1) and Ru(2) is found to be large but very similar for both the sites (about 3.7 eV) as expected for 4d-ruthenates (see the Supplemental Material) [33]. The large value of Δ_{CF} in comparison to Hund's coupling J_H (0.3−0.5 eV), typical for 4d systems, suggest the importance of t_{2g} states for magnetism. The distortion of Ru(1)O_6 and Ru(2)O_6 octahedra will further split the t_{2g} levels. To identify this, we have constructed a low energy model Hamiltonian where Ru(1) and Ru(2) t_{2g} orbitals are retained in the basis and the rest of the orbital degrees of freedom are downfolded. The calculated onsite energies of the Ru(1) and Ru(2) t_{2g} states including the oxygen covalency, not only reveal that the distortion of the octahedra lifts the degeneracy of the t_{2g} states but also this splitting is markedly different for Ru(1) and Ru(2)(Fig. 6). For Ru(1), a pair of Ru t_{2g} states are nearly degenerate and is lower in energy from the other singly degenerate t_{2g} state by about 0.4 eV. The situation is quite different at the Ru(2) site where all the levels are split by a similar amount $\sim$0.15 eV. Such a splitting will promote orbital ordering at the Ru(1) site where four electrons will occupy the low lying t_{2g} states underscoring Hund's exchange and complete quenching of moments. Ru(2) sites will host a moment of 2 μ_B following Hund's rule in the t_{2g} manifold. Interestingly, due to large direct hopping between Ru(1) and Ru(2) ions in the trimer, nonmagnetic Ru(1) will facilitate strong antiferromagnetic superexchange between the pair of $S = 1$ Ru(2) ions leading to the formation of a dimer.

We have carried out spin-polarized GGA+U (U = Coulomb correlation) calculations for a ferromagnetic configuration of Ru(1) and Ru(2) spins. Our results (see the Supplemental Material [33]) are consistent with the above picture of orbital ordering, where the moments at the Ru(1)

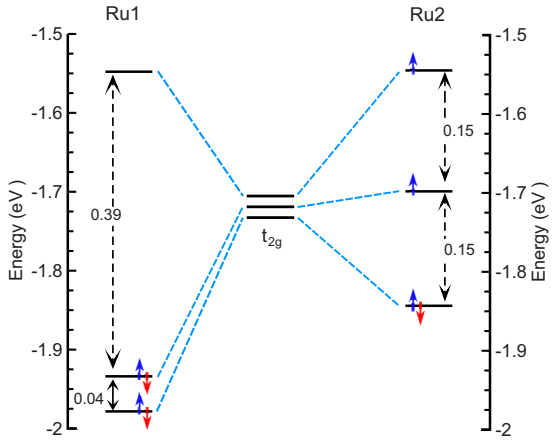

FIG. 6. Splitting of t_{2g} levels in the Ru(1) and Ru(2) octahedra. The large separation (0.39 eV) between the highest and the low-lying t_{2g} states of Ru(1) makes the total spin moment zero.

site is small whereas the Ru(2) site hosts a moment slightly less than 2 μ_B due to oxygen covalency. Finally, we have calculated the magnetic ground state within the GGA+U+SOC (SOC = spin orbit coupling) by considering all symmetry allowed magnetic structures corresponding to the wave vector $\mathbf{k} = (000)$. The details of our calculations are included in the Supplemental Material [33], and the predicted magnetic structure with moments aligned along the a direction is in excellent agreement with that obtained from the NPD experiment. Interestingly, below T_N, the ordered moment at the Ru(1) should vanish naturally from symmetry considerations.

D. Inelastic neutron scattering

INS experiments were performed to probe the nature of magnetic excitations. Figure 7(a) shows the 2D color plot of the phonon corrected neutron scattering data at 5 K with an incident energy of $E_i = 100$ meV, which contains bands of scattering intensity between the energy transfer, $\hbar\omega = 18$ and 42 meV. At larger $|\vec{Q}|$, the intensity is stronger indicating the presence of a phonon mode at the same energy as the magnetic excitations, suggesting a coupling between lattice and electronic degrees of freedom. The peak intensities at 18 and 42 meV also fall off rapidly with increasing temperature and vanishes above T_N. This implies that the low-$|\vec{Q}|$ scattering between 15 and 45 meV is related to the spin-wave excitations of the AFM state.

We further analyze the spin-wave excitation spectra using the SpinW package [38]. The spin Hamiltonian of the system can be constructed as

$$\mathcal{H} = \sum_{ij} J_{ij}(\vec{S}_i \cdot \vec{S}_j) + \sum_i \vec{A}_\zeta \left(S_i^\zeta\right)^2. \quad (2)$$

Here, the first term represents the Heisenberg interaction term with J_{ij} being the strength of the interaction between i-th and j-th spins. The second term represents the spin anisotropy with ζ being the anisotropy direction. In the case of BRO, we only consider the interaction between the Ru(2) atoms, as Ru(1) does not contribute any ordered moment. For the simulation, we have used the $\mathbf{k} = (000)$ AFM structure along

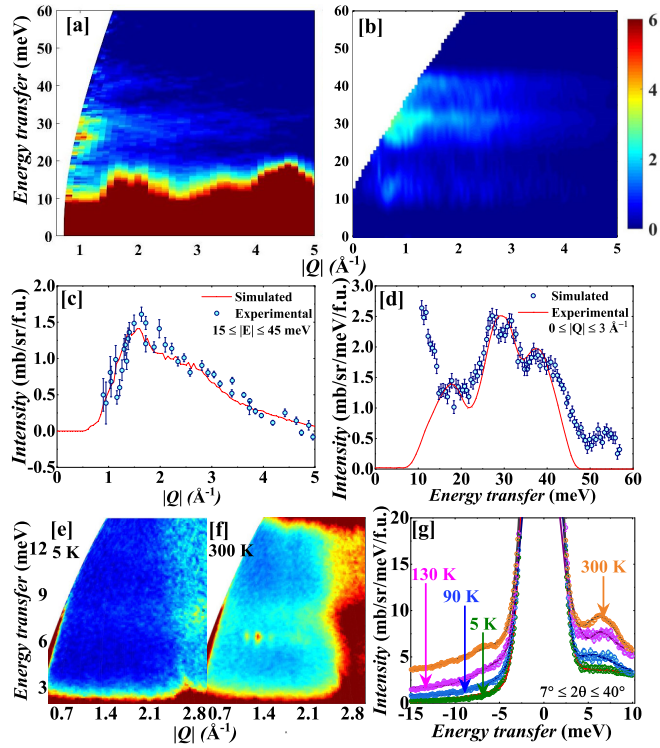

FIG. 7. Phonon corrected 2D color plots (momentum transfer versus energy transfer) from (a) INS experiment (at 5 K) and (b) simulated by the SpinW. (c) Experimental and (d) simulated scattering intensity as a function of $S(|\vec{Q}|)$ in the range of the $\hbar\omega$ summed over 15-45 meV and as a function of $\hbar\omega$ in the range of $0 \leqslant |\ Q\ | \leqslant 3$ Å^{-1} (low range of $S(|\vec{Q}|)$) respectively. 2D color plots of the low energy INS intensity at (e) 5 K and (f) 300 K respectively. (g) Scattering intensity versus $\hbar\omega$ plots indicating the opening of a spin-gap.

with the a being the easy axis of anisotropy. Because the magnetic structure is purely AFM without any spin canting, it is likely that J_1, J_2 and J_3 will all be positive (i.e., AFM). We have properly combined the energy resolution function of the neutron spectrometer ($E_i = 100$ meV) in the SpinW calculation. For the simulation of the INS intensity, we started with the J values predicted by GGA and GGA+U calculations, which are shown in Table I. The simulated color plot is shown in Fig. 7(b). The energy cut between 15 to 45 meV [Fig. 7(c)] shows a clear drop in intensity for $|\vec{Q}| > 1.5$ Å^{-1}. The $|\vec{Q}|$ integrated intensity between 0 to 3 Å^{-1} shows three distinct peaks in the simulated data centered around 18, 30, and 36 meV [Fig. 7(d)], which are also observed experimen-

TABLE I. Magnetic exchange parameters (J_1, J_2 and J_3), anisotropy energy (A_a) and the magnetic moment at the Ru sites as obtained from DFT calculations (GGA and GGA+U) and simulated and/or experimental data of the present work.

Model	J_1	J_2	J_3	A_a	Ru(1)	Ru(2)
		(meV)			Moment (μ_B)	
GGA	29.7	7.4	2.2		0.0	0.88
GGA+U	22.8	2.6	0.98		0.0	1.31
Simul./Exp.	21	9	1	−5.7	0.0	0.887(2)

tally. The J values obtained from the SpinW simulation (J_1, J_2 and $J_3 = 21$, 9, and 1 meV, respectively) are close to the DFT values (see Table I). In line with the DFT result, all J_i's are AFM with the magnitude of intratrimer J_1 being the largest.

The most striking feature of the INS study is the presence of a low energy excitation centered around 7 meV above T_N [Figs. 7(e)–7(g)]. The intensity associated with the peak at 7 meV is found to be the strongest at 300 K [Fig. 7(g)], and it slowly dies down as the temperature is reduced through T_N. A similar kind of low energy (∼10 meV) excitation has been observed at 6.8 K in $Tl_2Ru_2O_7$, which is assigned to the formation of a Haldane gap [26]. In the present case, BRO has zig-zag chains with bond alternation. If we use the values of J_1 and J_2 obtained from our SpinW simulation of the INS data, α turns out to be 0.4, which is above α_c. This indicates that in the Affleck-Haldane phase diagram [1,17], the system lies in the spin-dimer state rather than a Haldane state (see the right panel of Fig. A of the Supplemental Material [33]).

E. Magnetic susceptibility

We have studied the $\chi(T)$ data over a wide range of temperature between 2 and 780 K (Fig. 8). The χ ($=M/H$, M and H are the dc magnetization and the applied magnetic field, respectively) versus T data show a humplike feature around 180 K, followed by a sharper drop below about 100 K. This broad humplike feature is characteristic of many other $A_4X_3O_{10}$ (A = Sr, Ba and X = transition metal) compounds having a similar crystal structure, such as $Ba_4Mn_3O_{10}$ and $Sr_4Mn_3O_{10}$ [51]. The data can be fitted with a Curie-Weiss law between 484 and 780 K, where we get a paramagnetic Weiss temperature $\theta_W = -437$ K and effective paramagnetic moment $\mu_{eff} = 2.7\ \mu_B$/Ru. High-temperature paramagnetic susceptibility indicates that both the Ru ions stay in the 4+ state with effective $S = 1$, where the e_g levels are empty and 4 electrons occupy the low lying t_{2g} levels due to an octahedral crystal field. This is consistent with the findings of Klein *et al.* [29]. Our $\chi(T)$ data starts to deviate from the Curie-Weiss law below 484 K indicating the development of short-range correlations.

We further checked our result by fitting the $\chi(T)$ data between 300 and 120 K using a model proposed by Suzuku and Suga [50] for the system having alternating bond chains [Fig. 8(b)]. In the dimerized state of the bond-alternating chain, one can write,

$$\chi_{\text{dimer}}(T) = \frac{2\beta(g\mu_B)^2 N_A(\rho_t + 5\rho_q)}{1 + (\lambda - 1)\eta J_1(\rho_t + 5\rho_q)},$$
$$\beta = (k_B T)^{-1},$$
$$\eta = \frac{1-\alpha}{1+\alpha},$$
$$\rho_t = \exp(J_1\beta)/Z,$$
$$\rho_q = \exp(-J_1\beta)/Z,$$
$$Z = \exp(2J_1\beta) + 3\exp(J_1\beta) + 5\exp(-J_1\beta).$$

Here λ is a correlation parameter determined by the self-consistency equation derived from the fluctuation-dissipation theorem. To fit our susceptibility data [Fig. 8(b)], we have used a slightly modified form of the fitting function:

$$\chi_{\text{fit}} = \chi_{\text{dimer}} + \chi_0. \quad (3)$$

Here, χ_0 is a small temperature independent term. We fitted the curve between 115 and 300 K, and obtained, $\chi_0 = 3.3\times10^{-4} \pm 2\times10^{-8}$ emu/mol, λ = -0.375 ± 0.0004, $\eta = 0.415 \pm 0.0008$ (gives $\alpha = 0.413$) and $J_1 = 19.64 \pm 0.078$ meV. The fit provides us with the value of α to be 0.41(5), in excellent agreement with the value obtained from our INS data. Considering $\alpha = 0.4$ for BRO, the dimeric spin gap obtained from the $\Delta - \alpha$ phase diagram (see Fig. 1 of Ref. [17] and Fig. A of the Supplemental Material [33]) is found to be 6.3 meV, which is quite close to the 7-meV peak observed in the INS data [Fig. 7(g)]. The intensity of the dimeric peak in the INS data decreases with decreasing temperature, which can be ascribed to the development of interchain interactions that eventually leads to a Néel phase at low temperature [52].

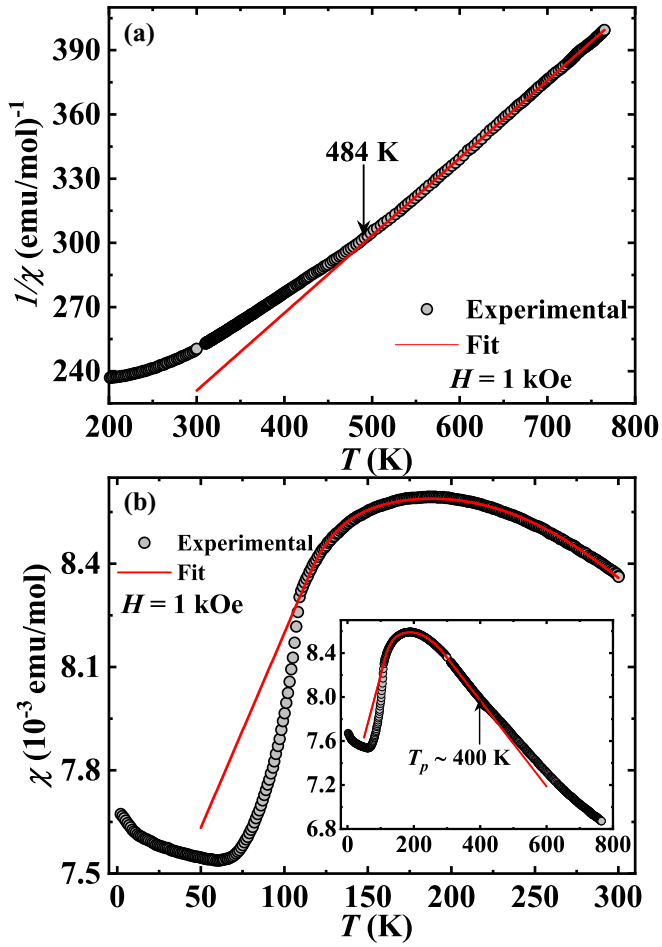

FIG. 8. (a) High-temperature inverse susceptibility versus temperature (200–780 K) of BRO. The sample follows a Curie-Weiss law between 780 and 484 K (solid line). Below 484 K, the spin dimer formation starts and the susceptibility deviates from the Curie-Weiss law. (b) Temperature dependence of the magnetic susceptibility. The solid red line represents the fitting of the $\chi(T)$ data between 300 and 120 K using the model proposed by Suzuku and Suga. [50] In the inset of (b), the fitted curve is extrapolated above 300 K, and it deviates from the experimental data at around 400 K.

Equation (3) fits the $\chi(T)$ data well up to 400 K [inset of Fig. 8(b)]. This indicates that the dimeric phase, with zero moment at the Ru(1) site, exists up to about 400 K from above T_N.

IV. CONCLUSIONS

In conclusion, we have found an $S = 1$ Ru-spin dimer state [53] in the bond alternating zig-zag chain system BRO, and the formation of dimers is well within the regime of the parameter α, where the hidden topological order is already broken. Notably, α is close to that obtained for the case of $Ni(C_9H_{24}N_4)NO_2(ClO_4)$ [NTENP], which is also a bond-alternating dimer [17]. The Ru(2) dimers in BRO are superexchange mediated through orbital-order-driven nonmagnetic Ru(1) ions. Our detailed combined experimental and theoretical study establishes that the exotic magnetic phase diagram of this fascinating compound containing [Ru(2)-Ru(1)-Ru(2)]-trimeric units, emerges from a paramagnetic phase ($S = 1$ for both Ru(1) and Ru(2)) at high-temperature (above about 500 K) into a spin dimer phase ([Ru(2)-Ru(2)] type $S = 1$) below about 400 K promoted by orbitally ordered nonmagnetic Ru(1). The system eventually orders below 107 K by the interdimer magnetic interaction leading to a long-range AFM ground state.

ACKNOWLEDGMENTS

The work was supported by the India-RAL collaborative project (SR/NM/Z-07/2015). We would like to thank the ISIS Facility for beam time on MERLIN, and WISH RB1610476 [54], RB1868025 [55]. J.S. wishes to acknowledge the EU's Horizon 2020 research and innovation program under the Marie Skłodowska-Curie Grant Agreement (No. 665593) awarded to the STFC, United Kingdom. D.T.A. thanks the Royal Society of London for Newton Advanced Fellowship funding between the UK and China and International Exchange funding between UK and Japan. I.D. thanks DST-TRC and the Science and Engineering Research Board (SERB) India (Project No. EMR/2016/005925) for support. We thank Dr. G. B. G. Stenning, ISIS Materials Characterization Laboratory for help with the magnetization and heat capacity measurements.

[1] I. Affleck, J. Phys.: Condens. Matter **1**, 3047 (1989).
[2] H.-J. Mikeska and A. K. Kolezhuk, in *Quantum Magnetism*, edited by U. Schollwöck, J. Richter, D. J. J. Farnell, and R. F. Bishop (Springer, Berlin, 2004), pp. 1–83.
[3] T. Sakai and M. Takahashi, Phys. Rev. B **43**, 13383 (1991).
[4] F. Pollmann, E. Berg, A. M. Turner, and M. Oshikawa, Phys. Rev. B **85**, 075125 (2012).
[5] S. P. Strong and A. J. Millis, Phys. Rev. Lett. **69**, 2419 (1992).
[6] F. Delgado, C. D. Batista, and J. Fernández-Rossier, Phys. Rev. Lett. **111**, 167201 (2013).
[7] D. E. Cox and V. J. Minkiewicz, Phys. Rev. B **4**, 2209 (1971).
[8] W. J. L. Buyers, R. M. Morra, R. L. Armstrong, M. J. Hogan, P. Gerlach, and K. Hirakawa, Phys. Rev. Lett. **56**, 371 (1986).
[9] T. Kennedy and H. Tasaki, Commun. Math. Phys. **147**, 431 (1992).
[10] H. Tasaki, Phys. Rev. Lett. **121**, 140604 (2018).
[11] S. Chattopadhyay, D. Jain, V. Ganesan, S. Giri, and S. Majumdar, Phys. Rev. B **82**, 094431 (2010).
[12] A. F. Albuquerque, C. J. Hamer, and J. Oitmaa, Phys. Rev. B **79**, 054412 (2009).
[13] M. T. Batchelor, X.-W. Guan, and N. Oelkers, Phys. Rev. B **70**, 184408 (2004).
[14] W. Chen, K. Hida, and B. C. Sanctuary, Phys. Rev. B **67**, 104401 (2003).
[15] H. Fan, V. Korepin, and V. Roychowdhury, Phys. Rev. Lett. **93**, 227203 (2004).
[16] R. R. P. Singh and M. P. Gelfand, Phys. Rev. Lett. **61**, 2133 (1988).
[17] A. Zheludev, T. Masuda, B. Sales, D. Mandrus, T. Papenbrock, T. Barnes, and S. Park, Phys. Rev. B **69**, 144417 (2004).
[18] Y. Narumi, M. Hagiwara, M. Kohno, and K. Kindo, Phys. Rev. Lett. **86**, 324 (2001).
[19] M. Hagiwara, L. P. Regnault, A. Zheludev, A. Stunault, N. Metoki, T. Suzuki, S. Suga, K. Kakurai, Y. Koike, P. Vorderwisch, and J.-H. Chung, Phys. Rev. Lett. **94**, 177202 (2005).
[20] M. A. Prosnikov, A. N. Smirnov, V. Y. Davydov, R. V. Pisarev, N. A. Lyubochko, and S. N. Barilo, Phys. Rev. B **98**, 104404 (2018).
[21] S. Ma, C. Broholm, D. H. Reich, B. J. Sternlieb, and R. W. Erwin, Phys. Rev. Lett. **69**, 3571 (1992).
[22] Y. Narumi, K. Kindo, M. Hagiwara, H. Nakano, A. Kawaguchi, K. Okunishi, and M. Kohno, Phys. Rev. B **69**, 174405 (2004).
[23] M. Hälg, D. Hüvonen, T. Guidi, D. L. Quintero-Castro, M. Boehm, L. P. Regnault, M. Hagiwara, and A. Zheludev, Phys. Rev. B **92**, 014412 (2015).
[24] R. Kumar, T. Dey, P. M. Ette, K. Ramesha, A. Chakraborty, I. Dasgupta, J. C. Orain, C. Baines, S. Tóth, A. Shahee, S. Kundu, M. Prinz-Zwick, A. A. Gippius, N. Büttgen, P. Gegenwart, and A. V. Mahajan, Phys. Rev. B **99**, 054417 (2019).
[25] H. Wu, Z. Hu, T. Burnus, J. D. Denlinger, P. G. Khalifah, D. G. Mandrus, L.-Y. Jang, H. H. Hsieh, A. Tanaka, K. S. Liang, J. W. Allen, R. J. Cava, D. I. Khomskii, and L. H. Tjeng, Phys. Rev. Lett. **96**, 256402 (2006).
[26] S. Lee, J.-G. Park, D. T. Adroja, D. Khomskii, S. Streltsov, K. A. McEwen, H. Sakai, K. Yoshimura, V. I. Anisimov, D. Mori, R. Kanno, and R. Ibberson, Nat. Mater. **5**, 471 (2006).
[27] C. Dussarrat, F. Grasset, R. Bontchev, and J. Darriet, J. Alloys Compds. **233**, 15 (1996).
[28] A. H. Carim, P. Dera, L. W. Finger, M. Mysen, C. T. Prewitt, and D. G. Schlom, J. Sol. Stat. Chem. **149**, 137 (2000).
[29] Y. Klein, G. Rousse, F. Damay, F. Porcher, G. André, and I. Terasaki, Phys. Rev. B **84**, 054439 (2011).
[30] G. Radtke, A. Saúl, Y. Klein, and G. Rousse, Phys. Rev. B **87**, 054436 (2013).
[31] S. V. Streltsov and D. I. Khomskii, Phys. Rev. B **86**, 064429 (2012).
[32] T. Igarashi, Y. Nogami, Y. Klein, G. Rousse, R. Okazaki, H. Taniguchi, Y. Yasui, and I. Terasaki, J. Phys. Soc. Jpn. **82**, 104603 (2013).
[33] See Supplemental Material at http://link.aps.org/supplemental/10.1103/PhysRevB.103.144431 which contains supporting text

and four figures important for the main paper. Details of magnetization and heat capacity measurements, magnetic symmetry analysis for Neutron powder diffraction data and non-spin polarized and spin-polarized results of DFT analysis are reported in the Supplemental Material. Schematic representation of valence bond state is also shown in the Supplemental Material.

[34] I. Affleck and F. D. M. Haldane, Phys. Rev. B **36**, 5291 (1987).

[35] J. Rodrguez-Carvajal, Phys. B: Condens. Matter **192**, 55 (1993).

[36] S. R. Giblin, S. P. Cottrell, P. J. C. King, S. Tomlinson, S. J. S. Jago, L. J. Randall, M. J. Roberts, J. Norris, S. Howarth, Q. B. Mutamba, and N. J. Rhodes, Nucl. Instrum. Method. A **751**, 70 (2014).

[37] R. I. Bewley, R. S. Eccleston, K. A. McEwen, S. M. Hayden, M. T. Dove, S. M. Bennington, J. M. Treadgold, and R. L. S. Coleman, Physica B **385-386**, 1029 (2006).

[38] S. Toth and B. Lake, J. Phys.: Condens. Matter **27**, 166002 (2015).

[39] J. P. Perdew, K. Burke, and M. Ernzerhof, Phys. Rev. Lett. **77**, 3865 (1996).

[40] V. I. Anisimov, J. Zaanen, and O. K. Andersen, Phys. Rev. B **44**, 943 (1991).

[41] G. Kresse and J. Furthmüller, Phys. Rev. B **54**, 11169 (1996).

[42] G. Kresse and J. Hafner, Phys. Rev. B **47**, 558(R) (1993).

[43] P. E. Blöchl, Phys. Rev. B **50**, 17953 (1994).

[44] G. Kresse and D. Joubert, Phys. Rev. B **59**, 1758 (1999).

[45] O. K. Andersen and T. Saha-Dasgupta, Phys. Rev. B **62**, R16219(R) (2000).

[46] O. K. Andersen, T. Saha-Dasgupta, and S. Ezhov, Bull. Mater. Sci. **26**, 19 (2003).

[47] O. K. Andersen and O. Jepsen, Phys. Rev. Lett. **53**, 2571 (1984).

[48] O. K. Andersen, Phys. Rev. B **12**, 3060 (1975).

[49] P. Manuel, D. T. Adroja, P.-A. Lindgard, A. D. Hillier, P. D. Battle, W.-J. Son, and M.-H. Whangbo, Phys. Rev. B **84**, 174430 (2011).

[50] T. Suzuki and S. i. Suga, Phys. Lett. A **343**, 462 (2005).

[51] J. Sannigrahi, S. Chattopadhyay, A. Bhattacharyya, S. Giri, S. Majumdar, D. Venkateshwarlu, and V. Ganesan, J. Phys.: Condens. Matter **27**, 056001 (2015).

[52] S. Haravifard, A. Banerjee, J. van Wezel, D. M. Silevitch, A. M. dos Santos, J. C. Lang, E. Kermarrec, G. Srajer, B. D. Gaulin, J. J. Molaison, H. A. Dabkowska, and T. F. Rosenbaum, Proc. Natl. Acad. Sci. USA **111**, 14372 (2014).

[53] C. D. Ling, Z. Huang, B. J. Kennedy, S. Rols, M. R. Johnson, M. Zbiri, S. A. J. Kimber, J. Hudspeth, D. T. Adroja, K. C. Rule, M. Avdeev, and P. E. R. Blanchard, Phys. Rev. B **94**, 174401 (2016).

[54] D. T. Adroja and S. Majumdar, ISIS Data Home, Science & Technology Facilities Council, STFC Exp. No. RB1610476 (2016) doi:10.5286/ISIS.E.RB1610476.

[55] S. Majumdar, D. T. Adroja, and D. Khalyavin, ISIS Data Home, Science & Technology Facilities Council, STFC Exp. No. RB1868025 (2018) doi:10.5286/ISIS.E.RB1868025.